Detection of neutralino annihilation photons from external galaxies

E. A. Baltz

Department of Physics, University of California, Berkeley, CA 94720, USA

C. Briot, P. Salati, and R. Taillet

Laboratoire de Physique Théorique LAPTH, BP110, F-74941 Annecy-le-Vieux Cedex, France

J. Silk

Department of Astrophysics, Oxford University, Oxford OX1 3RH, United Kingdom

Draft Version of April 23, 2018

We consider neutralino annihilation in dense extragalactic systems known to be dominated by dark matter, in particular M87 and several local dwarf spheroidal galaxies. These annihilations can produce energetic gamma rays which may be visible to atmospheric Čerenkov telescopes. We explore the supersymmetric parameter space, and compute the expected flux of gamma—rays coming from these objects. It is shown that some parts of the parameter space lead to a signal observable with the next generation of Čerenkov telescopes, provided the supersymmetric dark matter has a clumpy structure, as may be expected in a hierarchical scenario for structure formation.

95.35.+d, 14.80.Ly, 95.85.Pw, 98.70.Rz

I. INTRODUCTION

One of the favorite candidates for the astronomical missing mass is a neutral weakly interacting particle. Such a species is predicted in particular by supersymmetry, a theory that is actively tested at accelerators. It is conceivable therefore that most of the dark matter in the halo of the Milky Way is made of such particles. The mutual annihilation of these so–called neutralinos would yield, among a few other indirect signatures, a flux of high–energy gamma–rays. The latter has been extensively studied in the literature [1–4]. It is unfortunately spoiled by the diffuse background produced by the spallation of cosmic–ray protons on the interstellar gas as discussed by Chardonnet et al. [5]. The distribution of molecular hydrogen inside the galactic ridge is not sufficiently well known to ensure an accurate prediction of the diffuse emission. This may obliterate a reliable interpretation of any putative gamma–ray excess in terms of supersymmetric dark matter.

We examine here the possibility of observing the gamma–ray signal from extra–galactic systems that contain large amounts of unseen matter. The giant elliptical galaxy M87, at the center of the Virgo Cluster, provides an excellent illustration. It is known to contain ten times more mass than our own Milky Way. Actually, X-ray observations of its ambient hot gas indicate that in the innermost 100 kpc, the mass reaches $\sim 10^{13}\,\mathrm{M}_\odot$. If neutralinos pervade this galaxy, a strong gamma–ray emission should be produced in the central region. Neutralino annihilation is associated to the gamma–ray flux at the Earth

$$\Phi_{\gamma}^{\text{susy}} = \frac{1}{4\pi} \langle \sigma v \rangle N_{\gamma} \int_{\log s} n_{\chi}^{2} ds \tag{1}$$

which, in the case of M87, is two orders of magnitude larger than for own galaxy. On the other hand, M87 is quite distant, about 15 Mpc away. It should therefore appear as a bright gamma—ray spot on the sky, extending for at most a few hundred square arcminutes. The detection of such a strong but localized source is well—suited for atmospheric Čerenkov telescopes (ACT) which can only monitor small portions of the sky at the same time but have very large effective collecting areas.

Dwarf spheroidal (dSph) galaxies are also suspected to contain significant amounts of dark matter. They orbit round the Milky Way and are intermediate in size between the globular clusters and larger systems such as the Magellanic clouds. The typical mass of dSph's is $\sim 1-4\times 10^7\,\mathrm{M}_\odot$ while their radii reach up to $\sim 1-2$ kpc. They are also closer than M87.

The gamma–ray flux (1) produced by annihilating species in M87 may be split into an astrophysical piece and a particle physics piece. The former term merely amounts to the integral along the line of sight of the dark matter density squared. It is approximately given by $M^2 R^{-5}$ where M denotes the mass contained within the radius R. In

the case of M87, that line of sight integral is $\sim 10\,\mathrm{M}_\odot^2~\mathrm{pc}^{-5}$ whereas it is $\sim 0.01-1\,\mathrm{M}_\odot^2~\mathrm{pc}^{-5}$ for dwarf spheroidals. This compares to the Milky Way value of $\sim 0.1\,\mathrm{M}_\odot^2~\mathrm{pc}^{-5}$ which corresponds to the inner 100 kpc. These rough estimates are improved in Sec. II where the distribution of matter inside M87 and the dSph systems is modeled together with the radial profile of the neutralino induced gamma–ray emission. The various backgrounds to the latter are discussed in Sec. III where a fiducial example is presented. In particular, the signal–to–noise ratio is derived as a function of the angular distance to the centers of the sources under scrutiny. The supersymmetric model is presented in Sec. IV. We then delineate in Sec. V the domain of neutralino masses and gamma–ray production cross sections which the next generation of atmospheric Čerenkov telescopes will explore. Both continuum and monochromatic channels are featured. We finally draw some conclusions in Sec. VI where we pay special attention to a possible clumpy structure of the neutralino distribution.

II. THE M87 AND DSPH SYSTEMS

The observed X-ray emission produced by clusters of galaxies such as Virgo results from the thermal bremsstrahlung that takes place in the hot diffuse intracluster gas (see [6] for a complete review). The temperature profile T(r) of the gas can be inferred from the spectrum of the X-ray radiation. The electron number density profile $n_e(r)$ can be obtained from the X-ray surface brightness

$$\Sigma(r) = \int n_e(\sqrt{r^2 + s^2}) L_X ds , \qquad (2)$$

where L_X denotes the X-ray luminosity of the plasma. The properties of the hot gas in the vicinity of M87 have been determined by Tsai [7]. The X-ray data are well fitted by

$$n_e(r) = n_o \frac{(r/a_1)^{-\alpha_1}}{1 + (r/a_1)^{\alpha_3}} \quad \text{and} \quad T(r) = T_\infty \left(\frac{r}{a_2 + r}\right)^{\alpha_2} ,$$
 (3)

with $n_0 = 4.31 \times 10^{-2}$ cm⁻³, $a_1 = 6.63$ kpc, $a_2 = 4.58 \times 10^5$ kpc, $\alpha_1 = 0.49$, $\alpha_2 = 0.114$, $\alpha_3 = 0.869$ and $T_{\infty} = 8.35 \times 10^7$ K. Assuming that the intracluster gas is in hydrostatic equilibrium, the total mass profile is given by

$$M(r) = -\frac{kTr}{G\mu m_n} \left(\frac{d\log n_e}{d\log r} + \frac{d\log T}{d\log r} \right) , \qquad (4)$$

where μm_p is the average mass of a particle in the gas. The total mass inside M87 reaches $8.4 \times 10^{11} \,\mathrm{M}_{\odot}$ at 10 kpc and $1.4 \times 10^{13} \,\mathrm{M}_{\odot}$ at 100 kpc. The contribution from the stars alone was obtained from B-band surface brightness profiles (see [7] and references therein). The dark matter component distribution is derived once the stars and the gas have been removed. Mappings of the X-ray emission in the Virgo cluster are consistent with the hypothesis that this system and its central galaxy contain non-baryonic dark matter. The ratio of the dark matter density to the baryonic matter density is also borrowed from [7]

$$\frac{\rho_{\rm DM}}{\rho_{\rm B}} = 0.15 \left(\frac{r}{1 \,\mathrm{kpc}}\right)^{1.5} . \tag{5}$$

The integral along the line of sight of $\rho_{\rm DM}^2$ is readily obtained.

Dwarf spheroidal (dSph) galaxies also seem to contain large amounts of unseen material [8]. Like globular clusters, dSph's have low luminosities of order $10^5 - 10^7 \,\mathrm{L}_\odot$ within an ill-defined radius r_t of a few kpc. Their structure also follows a King profile (see [9] for a review). If these systems are in virial equilibrium, a velocity dispersion σ of a few km/s translates into a mass

$$M_{\rm dSph} \simeq 2.3 \times 10^7 \,\rm M_{\odot} \, \left(\frac{\sigma}{10 \,\rm km/s}\right)^2 \, \left(\frac{1 \,\rm kpc}{r_t}\right) \,$$
 (6)

hence these systems have mass—to—light ratios that may reach ~ 200 . We have been interested here in four galaxies with exceptionally high M/L—values [10] and galactocentric distances less than 100 kpc. The dSph's featured in table I are Carina, Draco, Ursa Minor and Sextans. We have modeled their mass distributions with a one—component King profile [11] for which the phase space density is given by

Name			$M \over (10^6 \ {\rm M_{\odot}})$			c	$r_t ext{(kpc)}$	$\sigma_{ m th} \ ({ m km/s})$
Carina Draco Ursa Minor Sextans	1.8 ± 0.8 2.0 ± 0.9	245 ± 155 95 ± 43	$14.1 \pm 10.0 \\ 44.1 \pm 24.0 \\ 19.0 \pm 10.5 \\ 43.8 \pm 23.6$	72 ± 3 64 ± 5	10.2 ± 1.8 12.0 ± 2.4	$0.5 \\ 0.5$	2.18	7.6 11.8 12.8 8.8

TABLE I. These four dSph galaxies have very large M/L-values and are within 100 kpc from the Milky Way center. The luminosities L, mass-to-light ratios, total masses M, galactocentric distances d and concentrations c have been borrowed from [10]. The velocity dispersions $\sigma_{\rm obs}$ are those given by [13]. These systems have been modeled with King profiles as explained in the text. Consistency may be checked by comparing the resulting velocity dispersions $\sigma_{\rm th}$ with the observed values $\sigma_{\rm obs}$. Also indicated are the derived tidal radii r_t , in kpc.

$$f(E) \propto \exp\left(\frac{\phi_t - E}{\sigma^2}\right) - 1$$
 (7)

The stellar or particle energy per unit mass is denoted by $E = \phi + v^2/2$ while $\phi_t = \phi(r_t)$ is the potential at the tidal radius r_t of the dSph. Beyond that boundary, stars have enough energy to escape from the gravitational field of the system and are captured by the tidal field of the nearby Milky Way. The mass distribution ensues from the phase space density (7)

$$\rho(r) \propto \frac{\sqrt{\pi}}{4} \exp(u) \operatorname{erf}(\sqrt{u}) - \frac{\sqrt{u}}{2} - \frac{u^{3/2}}{3}$$
, (8)

where u denotes the ratio $\{\phi_t - \phi(r)\}/\sigma^2$ while erf is the error function. One component King models are completely determined once the velocity dispersion σ , the central density ρ_c and the ratio $\chi = \{\phi_t - \phi(0)\}/\sigma^2$ are specified. Any combination of these quantities suffices. The concentrations of the four dSph's under scrutiny are given in table I as determined by [10]. They are related to the tidal and core radii through

$$c = \log_{10} \left(\frac{r_t}{r_c} \right) , \qquad (9)$$

where the core radius r_c is defined as

$$r_c = \frac{3\sigma}{\sqrt{4\pi G\rho_c}} \ . \tag{10}$$

Values of the concentration of 0.5 and 1 respectively translate into the ratios $\chi=1.97$ and 4.85. Fixing the concentration allows for the determination of the density profile $\rho(r)/\rho_c$ as a function of the reduced radius r/r_c . The second input to our calculations is the dSph mass as given by the central values of table I. We finally set the average dSph density $\bar{\rho}_{\rm dSph}$ by requiring that the proper gravitational field of these galaxies is compensated, at their boundaries, by the tidal field of the Milky Way taken at perigalacticon. Assuming a logarithmic galactic potential implies that

$$\bar{\rho}_{\rm dSph} = f(e)\,\bar{\rho}_{\rm G} \,\,, \tag{11}$$

where the function f(e) depends on the orbital eccentricity of the satellite galaxy [12]

$$f(e) = \frac{1 + \left[(1+e)^2 / 2e \right] \ln \left[(1+e) / (1-e) \right]}{(1-e)^2} . \tag{12}$$

The average galactic density $\bar{\rho}_G$ is understood within the sphere centered on the Milky Way, with radius equal to the semimajor axis a of the dSph orbit. The corresponding mass is given by

$$M_{\rm G} = 1.1 \times 10^{10} \rm M_{\odot} \times a \ [kpc] \ .$$
 (13)

We set the semimajor axis a equal to the dSph galactocentric distance d. Eccentricities in the range between 0 and 1/2 are generally assumed. Here, their values were derived by requiring that the resulting velocity dispersions $\sigma_{\rm th}$ should be close to the observations – see table I. In the case of Carina and Draco, the eccentricity is e=0 while for Ursa Minor, a value of e=1/2 is appropriate. As regards Sextans, we simply imposed the equality between the dSph and galactic average densities, i.e., $\bar{\rho}_{\rm dSph} = \bar{\rho}_{\rm G}$, in order to get a velocity dispersion of 8.8 km/s, not too far from the measured value of 6.2 ± 0.8 km/s. Assuming relation (11) and a circular orbit would have lead to $\sigma_{\rm th}=9.9$ km/s. In modeling the dSph galaxies, we have adopted the point of view that these satellites contain large amounts of dark matter as implied by their high velocity dispersions. In the alternative explanation, the latter are the result of an ongoing tidal stripping. However, Oh et al. [13] showed that unbound but not yet dispersed systems have velocity dispersions fairly close to the values derived from the virial equilibrium. The large M/L-values of the four dSph systems at stake do not depend therefore on whether these galaxies are in equilibrium or are currently being torn apart. Notice finally that most of the putative neutralino-induced gamma-ray signal emitted by these dSph's is produced in the inner 10 arcmin as shown in the right panel of Fig. 1. It weakly depends on the actual boundaries of these systems.

III. THE GAMMA-RAY SIGNAL AND ITS BACKGROUNDS

The gamma–ray flux produced by a halo of dark matter particles may be computed as follows. First, for each set of supersymmetric parameters, we derived the thermally averaged annihilation cross section $\langle \sigma v \rangle_A$ into some channel A. Then, we used the Lund Monte Carlo [14] to compute the photon spectrum per annihilation from hadronization or decay processes, and we integrated over some specified threshold which depends on the atmospheric Čerenkov telescopes in question. Finally, we have summed over all channels to find the total photon spectrum from a given supersymmetric model. The volume production rate of gamma–rays is simply given by $n_\chi^2 \langle \sigma v \rangle N_\gamma$, where n_χ is the number density of annihilating particles and N_γ is the mean number of photons above the threshold. The corresponding flux at the Earth depends on the integral, along the line of sight, of the dark matter density squared

$$\Phi_{\gamma}^{\text{susy}} = \frac{1}{4\pi} \frac{\langle \sigma v \rangle N_{\gamma}}{m_{\chi}^2} \int_{\text{los}} \rho_{\chi}^2 ds , \qquad (14)$$

as well as on the gamma–ray production cross section $\langle \sigma v \rangle N_{\gamma}$ and the mass m_{χ} of the species.

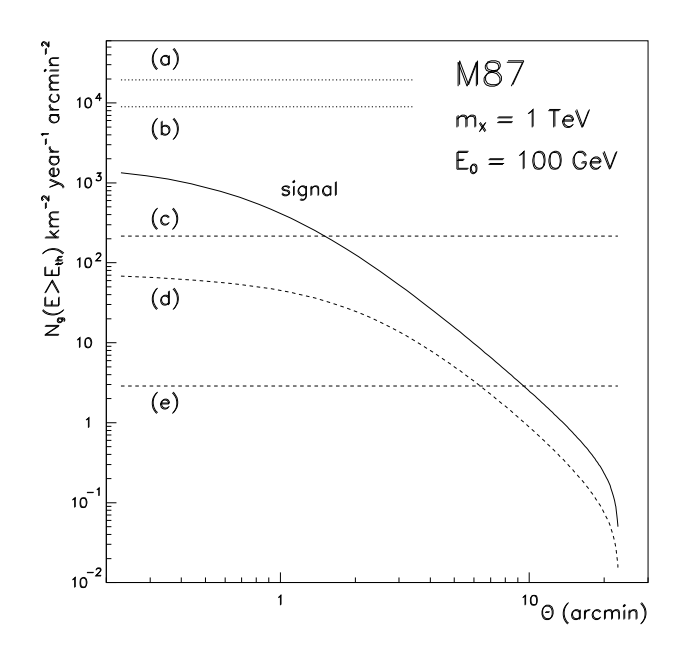
Atmospheric Čerenkov telescopes (ACT) offer the most promising method to detect gamma–rays with energies above 100 GeV. When passing through the atmosphere, incoming high–energy photons emit a Čerenkov radiation that is detected and analyzed to infer the energy and arrival direction of the primary gamma–ray. The performances of ACTs are determined by the surface of the optical reflectors used to collect the Čerenkov light, and the ability to reject the cosmic–ray induced background. A thorough analysis of these performances can be found in Aharonian [15]. We will simply model them by the effective collecting area $A_{\rm eff}$, a feature of the instrument that takes into account in particular the actual surface of detection together with the energy dependent detection efficiency.

The surface brightness $\mu_{\gamma}^{\text{susy}}$ of the source as seen by an ACT depends on the collecting area of the instrument and on the integration time T

$$\mu_{\gamma}^{\text{susy}} = \Phi_{\gamma}^{\text{susy}} A_{\text{eff}} T$$
 (15)

We plot the surface brightness in Fig. 1 for a collecting area $A_{\rm eff}=1~{\rm km^2}$ and for an entire year of effective observation. In the fiducial model taken here, the neutralino mass is $m_\chi=1~{\rm TeV}$ while the annihilation cross section has been set equal to $\langle \sigma v \rangle ~N_\gamma=10^{-25}~{\rm cm^3~s^{-1}}$. The surface brightness corresponds to the number of photons above a threshold of 100 GeV that are produced per square arcmin of the source. In the left panel, the giant galaxy M87 is featured whereas in the right panel, the four dSph satellites discussed in the previous section, i.e., Carina, Draco, Sextans and Ursa Minor are presented. The signal declines away from the centers of these systems. It follows the integral along the line of sight of the neutralino density squared – remember that $n_\chi=\rho_\chi/m_\chi$. Actually, we must take into account the finite angular resolution of the instrument. When the telescope is pointed towards the center of the object, photons coming from directions within the resolution cone also reach the detector. Thus, the relevant quantity to examine is the integral of the surface brightness $\mu_\chi^{\rm susy}$ over a disk centered on the source, with angular radius θ

$$N_{\rm s} = \int_0^\theta 2\pi\alpha \,\mu_{\gamma}^{\rm susy} \,d\alpha \ . \tag{16}$$



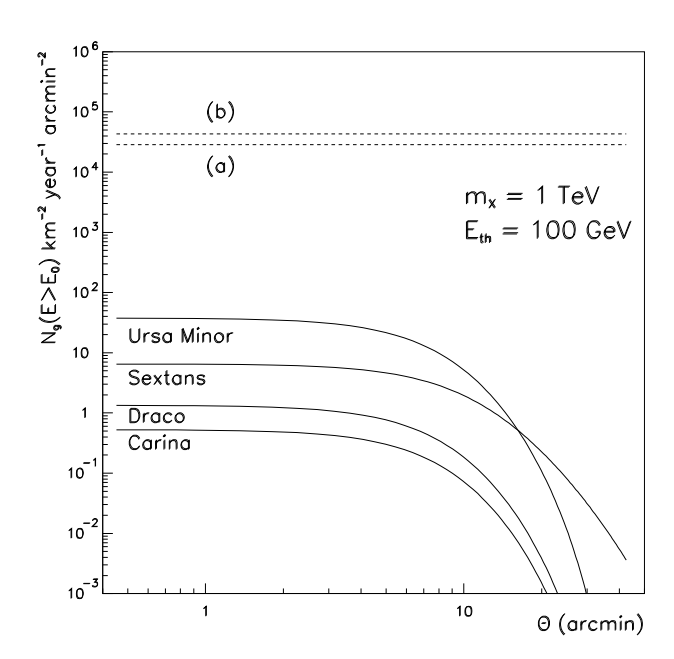


FIG. 1. The radial profiles of the neutralino–induced signal (solid curves) and of the various backgrounds (dotted and dashed lines) are plotted as a function of the angular distance to the source centers. A fiducial model with $m_{\chi}=1$ TeV and $\langle \sigma v \rangle_{\text{cont.}} N_{\gamma}=10^{-25}$ cm³ s⁻¹ is taken while a threshold of 100 GeV is assumed. In the left panel, the backgrounds are respectively labeled as (a): electronic; (b): hadronic; (c): extragalactic; (d): M87 and (e): Milky Way gamma–ray diffuse emissions. The right panel shows nearby dwarf spheroidal galaxies with exceptionally high M/L–values. The neutralino–induced signal is flat within 10 arcmin from the center. The total background is featured by the dashed line (g). Carina is the exception with a slightly larger value (f) dominated by the Milky Way diffuse emission. That system lies within the galactic ridge.

When the angular resolution of the ACT is good enough, the size of that circular region is generally specified by the requirement that the signal—to—noise ratio should be optimal.

The number of neutralino-induced source photons $N_{\rm s}$ should actually be compared to the background $N_{\rm bg}$, the origins of which are various. Would it be constant, this background could easily be removed from the signal. Actually, it follows Poisson statistics, and as such, it exhibits fluctuations of amplitude $\sqrt{N_{\rm bg}}$. These fluctuations have a smaller chance of being interpreted as a signal when the significance

$$S = \frac{N_{\rm s}}{\sqrt{N_{\rm bg}}} \tag{17}$$

is large. There are two main types of background events. First, an experimental background is due to hadronic and electronic cosmic–rays that impinge on the top of the atmosphere. The induced showers can be misinterpreted as gamma–ray events. Electrons make up the largest source of background insofar as their showers are of the electromagnetic type and cannot be disentangled from those generated by the impact of high–energy photons. The corresponding flux steeply decreases at high energy [16]

$$\Phi_{\rm e} = \left(6.4 \times 10^{-2} \,\text{GeV}^{-1} \,\text{cm}^{-2} \,\text{s}^{-1} \,\text{sr}^{-1}\right) \left(\frac{E}{1 \,\text{GeV}}\right)^{-3.3 \pm 0.2} , \qquad (18)$$

and leads to the background

$$\frac{dN_{\rm e}}{d\Omega}(E > E_0) = (1.9 \times 10^4 \,\mathrm{km}^{-2} \,\mathrm{yr}^{-1} \,\mathrm{arcmin}^{-2}) \left(\frac{E_0}{100 \,\mathrm{GeV}}\right)^{-2.3} . \tag{19}$$

In the left panel of Fig. 1, that electron induced background is featured by the dotted line (a). It is more than an order of magnitude larger than the neutralino-induced signal at maximum. It is also noticeably flat all over the source. Observations performed between 50 GeV and 2 TeV yield a hadron flux [17]

$$\Phi_{\text{had}} = \left(1.8 \,\text{GeV}^{-1} \,\text{cm}^{-2} \,\text{s}^{-1} \,\text{sr}^{-1}\right) \left(\frac{E}{1 \,\text{GeV}}\right)^{-2.75} . \tag{20}$$

Hadron-induced showers are more extended on the ground than those of the electromagnetic type. Stereoscopy is a powerful tool to discriminate hadrons from electrons and gamma-rays. The CAT experiment, for instance, has already achieved a rejection factor of one misidentified event over a sample of 600 showers generated by cosmic-ray hadrons [18]. Here, we have assumed an even better rejection factor, with only one misidentified hadron out of a thousand showers. This yields a hadron background

$$\frac{dN_{\text{had}}}{d\Omega}(E > E_0) = \left(8.7 \times 10^3 \text{ km}^{-2} \text{ yr}^{-1} \text{ arcmin}^{-2}\right) \left(\frac{E_0}{100 \text{ GeV}}\right)^{-1.75} . \tag{21}$$

which corresponds to the dotted line (b) of Fig. 1. Once again, that background is flat over M87. Next come the astrophysical sources of background. To commence, Sreekumar et al. [19] have measured an extragalactic component in the gamma—ray diffuse emission with the EGRET instrument on board the Compton gamma—ray observatory

$$\Phi_{\rm eg} = \left(7.32 \pm 0.34 \times 10^{-9} \,\mathrm{MeV^{-1} \,cm^{-2} \,s^{-1} \,sr^{-1}}\right) \left(\frac{E}{451 \,\mathrm{MeV}}\right)^{-2.10 \pm 0.03} . \tag{22}$$

This translates into the background (c)

$$\frac{dN_{\text{eg}}}{d\Omega}(E > E_0) = \left(2.1 \times 10^2 \,\text{km}^{-2} \,\text{yr}^{-1} \,\text{arcmin}^{-2}\right) \left(\frac{E_0}{100 \,\text{GeV}}\right)^{-1.1} . \tag{23}$$

In our fiducial example, the neutralino–induced signal exceeds the extragalactic background within ~ 1 arcmin from the center of M87. Then, we have modeled the gamma–ray diffuse emission from that giant elliptical galaxy itself. Local cosmic–rays interact with the cluster gas to produce high–energy photons that may potentially contaminate the signal. In the inner 10 kpc, the magnetic field of M87 is comparable to that of the Milky Way, with a magnitude ~ 1 μ G. It falls by a factor of ten outwards in the Virgo cluster, at a distance of ~ 100 kpc. Assuming that equipartition of energy holds between this magnetic field and the cosmic–rays that pervade M87 – just like in our own galaxy – we infer a gamma–ray emissivity of

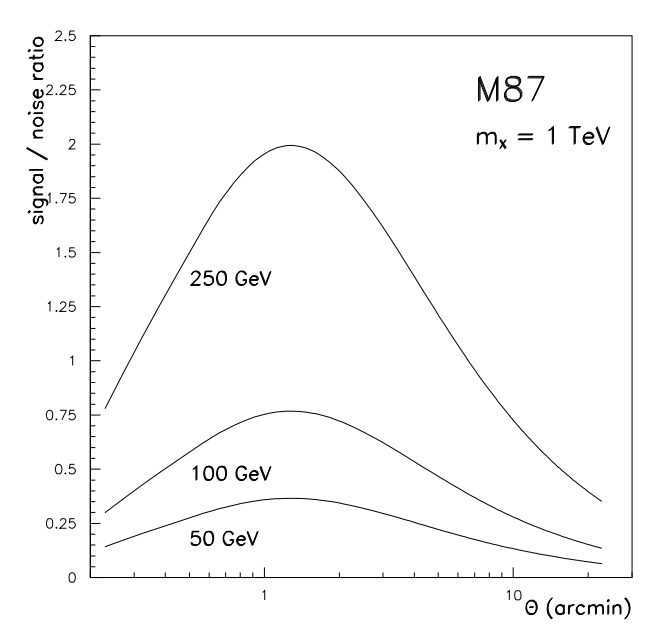
$$I_{\rm H}(E) = \left(2 \times 10^{-35} \,\mathrm{GeV^{-1} \,s^{-1} \,sr^{-1}}\right) \left(\frac{E}{1 \,\mathrm{TeV}}\right)^{-2.73} ,$$
 (24)

per hydrogen atom illuminated by high–energy protons. Once multiplied by the hydrogen column density across M87, it yields the in situ diffuse gamma–ray flux. We have assumed that hydrogen is the main constituent of the gas at the center of the Virgo cluster so that we have integrated the electron density, as derived in Sec. II, along the appropriate lines of sight. The gamma–ray emissivity as given by relation (24) is typical of the inner 10 kpc inside M87. It has been rescaled by the factor $\left\{1+(r/10\,\mathrm{kpc})^2\right\}^{-1}$ to account for the outward decrease of both the magnetic energy and cosmic–ray flux. The M87 gamma–ray diffuse background is presented as the dashed line (d) of Fig. 1. It falls outwards as a result of the combined decrease of the hydrogen column density and of the cosmic–ray flux. Finally, we have taken into account the Milky Way diffuse emission. We use hydrogen column densities inferred from the dust maps of [20]. A hydrogen column density of $1.69 \times 10^{20} \,\mathrm{H}$ cm⁻² in the direction of M87 corresponds to

$$\frac{dN_{\text{MW}}}{d\Omega}(E > E_0) = \left(2.8 \text{ km}^{-2} \text{ yr}^{-1} \text{ arcmin}^{-2}\right) \left(\frac{E_0}{100 \text{ GeV}}\right)^{-1.73} , \qquad (25)$$

and to the dashed line (e). The Milky Way component is the weakest source of background. Electrons and in a lesser extent hadrons – as long as rejection is efficient – dominate. In the right panel of Fig. 1, the total background is presented. It encompasses the various sources discussed above except a local diffuse emission. The dSph galaxies contain old stars and the acceleration mechanisms at work in the Milky Way are presumably less prevalent there. Even in the case of the brightest source, Ursa Minor, the signal is still three orders of magnitude below the background – see curve (g). Because Carina lies in the sky towards the galactic ridge, the hydrogen column density of the Milky Way is quite large, reaching a value of 8.7×10^{23} H cm⁻². The gamma–ray diffuse emission of our own galaxy dominates the background (f) in that specific case.

The significance S is presented in Fig. 2 for M87 (left panel) and in the case of Ursa Minor, the best dSph source (right panel). Should the signal be flat, both $N_{\rm s}$ and $N_{\rm bg}$ would be proportional to the surface of the sky monitored by



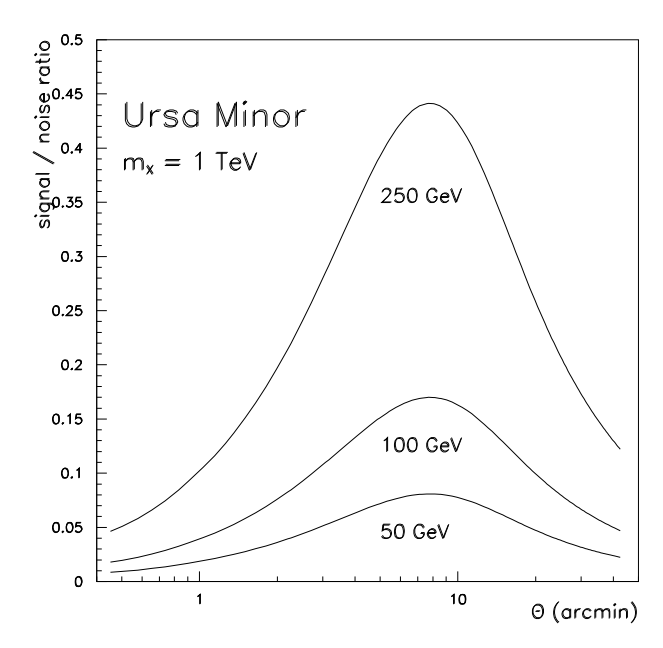


FIG. 2. Signal-to-noise ratio as a function of threshold and beam size. Again a fiducial model with $m_{\chi}=1$ TeV and $\langle \sigma v \rangle_{\rm cont.} N_{\gamma}=10^{-25}~{\rm cm}^3~{\rm s}^{-1}$ is taken, while a more realistic integration of 0.01 km² yr is now assumed. The left panel features the case of M87 for which the significance S peaks at an angular radius of ~ 1.4 arcmin. For the brightest dSph Ursa Minor (right panel), the optimal beam size is 7.7 arcmin. Three values of the threshold energy are presented.

the ACT. As a result, the signal–to–noise ratio would just increase like the angular radius θ of the observed region. In Fig. 2, it actually increases as the beam size opens up. Because the signal is not flat but weakens far from the source, the signal–to–noise ratio reaches a maximum and drops at larger radii. The ACT acceptance has been set equal to 0.01 km² yr. The neutralino mass is still 1 TeV whereas the gamma–ray production cross section $\langle \sigma v \rangle_{\rm cont.} N_{\gamma} = 10^{-25}$ cm³ s⁻¹ is the same for the three values of the threshold energy featured here. As the background is flat over the source, the signal–to–noise ratio always peaks at the same angular position. For M87, the significance is the largest for an angular aperture of ~ 1.4 arcmin. Because Ursa Minor is closer, the optimal beam size becomes 7.7 arcmin. As both the electronic and hadronic backgrounds weaken with the gamma–ray energy, the magnitude of the maximum increases with the threshold as is clear in both panels. For M87 and a 50 GeV threshold, the significance reaches a value of ~ 0.4 whereas for 250 GeV, the peak value increases up to 2. In the case of Ursa Minor, the variations of the significance are just the same. Should the acceptance be 1 km² yr, these signal–to–noise ratios would be rescaled up by an order of magnitude.

IV. EXPLORING THE SUSY PARAMETER SPACE

We have explored the Minimal Supersymmetric Standard Model (MSSM). This framework has many free parameters, but with reasonable assumptions the set of parameters is reduced to seven: the Higgsino mass parameter μ , the gaugino mass parameter M_2 , the ratio of the Higgs vacuum expectation values $\tan \beta$, the mass of the CP-odd Higgs boson m_A , the scalar mass parameter m_0 and the trilinear soft SUSY-breaking parameters A_b and A_t for third generation squarks. The only constraint from supergravity that we imposed is gaugino mass unification, though the relaxation of this constraint would not significantly alter our results. For a more detailed description of these models, see Refs. [21,22].

The lightest stable supersymmetric particle in most models is the lightest of the neutralinos, which are superpositions of the superpartners of the gauge and Higgs bosons. We used the one-loop corrections for the neutralino and chargino masses given in Ref. [23]. For the Higgs bosons we used the leading log two-loop radiative corrections, calculated within the effective potential approach given in Ref. [24]. We made thorough random scans of the model parameter space, with overall limits of the seven MSSM parameters as given in Table II.

Each model was examined to see if it is excluded by the most recent accelerator constraints. The most important

Parameter	μ	M_2	$\tan \beta$	m_A	m_0	A_b/m_0	A_t/m_0
Unit	${ m GeV}$	${ m GeV}$	1	${ m GeV}$	${ m GeV}$	1	1
Min	-50000	-50000	1.0	0	100	-3	-3
Max	50000	50000	60.0	10000	30000	3	3

TABLE II. The ranges of parameter values used in our scans of the MSSM parameters. In total, we used approximately 116,000 models that are not excluded by current accelerator constraints.

of these are the LEP bounds [25] on the lightest chargino mass

$$m_{\chi_1^+} > \begin{cases} 91 \text{ GeV} &, & |m_{\chi_1^+} - m_{\chi_1^0}| > 4 \text{ GeV} \\ 85 \text{ GeV} &, & \text{otherwise} \end{cases}$$
 (26)

and on the lightest Higgs boson mass $m_{H_2^0}$ (which ranges from 72.2–88.0 GeV depending on $\sin(\beta - \alpha)$ with α being the Higgs mixing angle) and the constraints from $b \to s\gamma$ [26].

For each allowed model, the relic density of neutralinos $\Omega_\chi h^2$ was calculated, where Ω_χ is the density in units of the critical density and h is the present Hubble constant in units of 100 km s⁻¹ Mpc⁻¹. We used the formalism of Ref. [27] for resonant annihilations, threshold effects, and finite widths of unstable particles and we included all two-body tree-level annihilation channels of neutralinos. We also included the so-called coannihilation processes between all neutralinos and charginos in the relic density calculation according to the analysis of Edsjö and Gondolo [21]. Present observations favor $h=0.6\pm0.1$, and a total matter density $\Omega_M=0.3\pm0.1$, of which baryons may contribute 0.02 to 0.08 [28]. However, we only required that $\Omega_\chi h^2 \leq 0.5$. We were also interested in models where neutralinos are not the only component of dark matter. In models with $\Omega_\chi h^2 \leq 0.025$, we rescaled the relevant halo densities by a factor $\Omega_\chi h^2/0.025$ to account for the fact that a supplemental source of dark matter is required in such models.

V. FLUX OF GAMMA-RAYS FROM NEUTRALINO ANNIHILATION

We now present the results of the scans over the supersymmetric parameter space. We first made scatter plots of the continuum gamma–ray production rate $\langle \sigma v \rangle_{\rm cont.}$ N_{γ} versus the neutralino mass m_{χ} , for three gamma–ray thresholds $E_{\rm th}=50,\,100$ and 250 GeV. The results are presented in Fig. 3, along with the 3– σ detection limit of the signal from M87, for a typical exposure of 0.01 km² yr. This acceptance corresponds to the next generation of ACTs. The HESS project [29] for instance should reach a threshold of 40 GeV for a collecting area of 300 m by 300 m. Its angular resolution should be 0.1°. We have assumed a generous 0.1 yr integration time which would correspond to a few months of continuous observation. This compares to the VERITAS project which should be sensitive to the energy range extending from 50 GeV up to 50 TeV. A collecting area of 10,000 m² is expected at 100 GeV, increasing by an order of magnitude for TeV photons. VERITAS should reach an angular resolution of 5 arcmin at 100 GeV [30]. As shown in the left panel of Fig. 2, the optimal beam size is 1.4 arcmin in the direction of M87. For a 6 arcmin angular resolution and a 50 GeV threshold, the significance drops down to S=0.2. A 3– σ detection level translates therefore into the gamma–ray production cross section $\langle \sigma v \rangle_{\rm cont.}$ $N_{\gamma}=1.5\times10^{-24}$ cm³ s⁻¹ for a 1 TeV neutralino. The heavy solid line in the upper–left panel of Fig. 3 corresponds to a sensitivity level of

$$\langle \sigma v \rangle_{\text{cont.}} N_{\gamma} \ge 1.5 \times 10^{-26} \,\text{cm}^3 \,\text{s}^{-1} \, \left(\frac{m_{\chi}}{100 \,\text{GeV}}\right)^2 .$$
 (27)

The region below that line will not be accessible, even with the next generation of Čerenkov telescopes. When the threshold increases to 100 and 250 GeV, the sensitivity respectively reaches down a level of 7.2×10^{-27} and 2.8×10^{-27} cm³ s⁻¹. Notice that even for a 250 GeV threshold, the number of background photons collected within 6 arcmin from the center of M87 amounts to $\sim 4{,}600$ particles. A $3-\sigma$ signal corresponds to ~ 200 additional gamma–rays from that hot spot. For a 50 GeV threshold, $\sqrt{N_{\rm bg}} \sim 1.4 \times 10^5$ photons whereas $N_{\rm s} \sim 1{,}100$ photons.

In Fig. 4, we present the results for the gamma–ray lines. We considered the two processes $\chi\chi \to \gamma\gamma$ and $\chi\chi \to Z^0\gamma$. The photon energy in the 2γ process is clearly $E_{\gamma} = m_{\chi}$, while in the $Z^0\gamma$ reaction the photon energy is

$$E_{\gamma} = m_{\chi} - \frac{m_Z^2}{4m_{\chi}} . \tag{28}$$

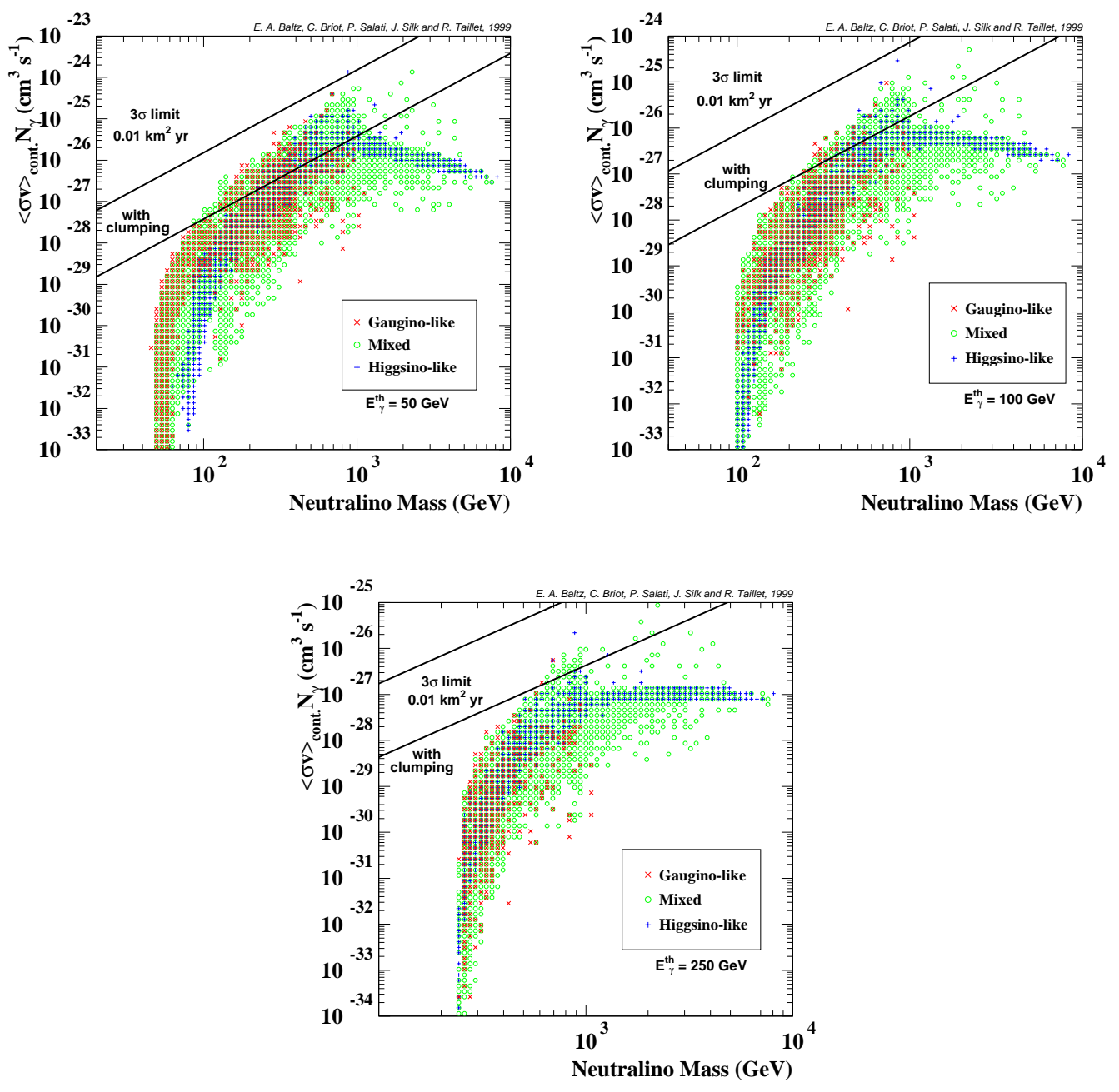


FIG. 3. Annihilation rates in the continuum channels. Three thresholds are illustrated, $E_{\rm th}=50$, 100 and 250 GeV. Considering M87 as the source, the 3- σ detection limits for exposures of 0.01 km² yr are also presented. The regions below the higher heavy solid lines will not be accessible, even with the next generation of Čerenkov telescopes. The lower solid lines show the region of accessibility if annihilation rate is enhanced by a factor of 40 due to clumpiness.

As in Fig. 3, we also present detection limits. The left panel features the two gamma–ray line whereas the right panel presents the $Z^0\gamma$ process. The sensitivity limits are identical for both lines at high energy, *i.e.*, for massive neutralinos. In the case of the $Z^0\gamma$ line, the photon energy becomes vanishingly small as the neutralino mass m_χ tends to $m_Z/2$. Because the signal becomes swamped inside a very strong low–energy gamma–ray background, the sensitivity drops completely and the detection limit of the right panel exhibits a sharp increase around $m_Z/2$. Below that threshold, the $Z^0\gamma$ process is no longer kinematically allowed. There is an additional restriction arising from the energy threshold $E_{\rm th}$ of the Čerenkov telescope itself. Requiring that $E_{\gamma} > E_{\rm th}$ implies that the neutralino mass should exceed

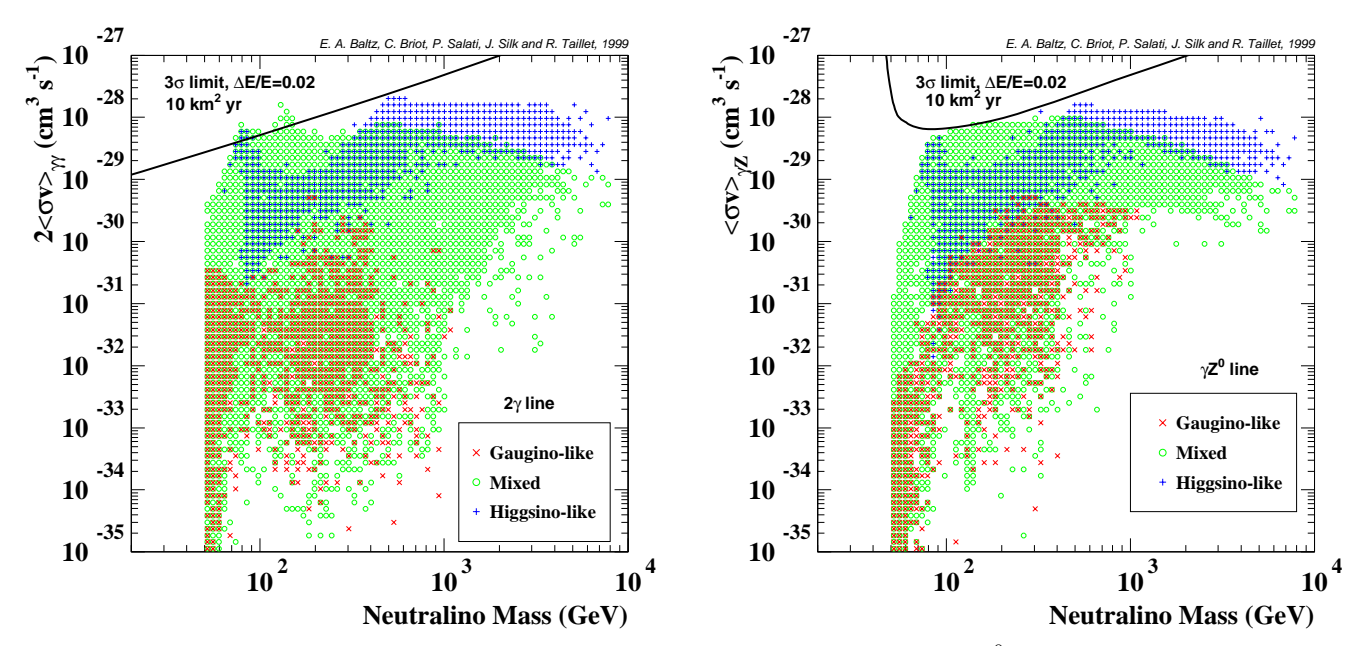


FIG. 4. Annihilation rates in the monochromatic channels. (left): $2-\gamma$ line. (right): $Z^0\gamma$ line. Both processes are present with their $3-\sigma$ detection limits for a 10 km² yr exposure towards M87 together with an energy resolution of $\Delta E/E = 0.02$.

$$m_{\chi} \ge \frac{E_{\rm th} + \sqrt{m_Z^2 + E_{\rm th}^2}}{2} \ .$$
 (29)

For a 50 GeV threshold, this translates into $m_{\chi} \geq 77$ GeV. We find that the lines are much more difficult to detect. The sensitivities presented here correspond to an exposure of 10 km² yr and an energy resolution $\Delta E/E = 0.02$, both of which are unreasonable with today's detectors.

VI. DISCUSSION AND CONCLUSIONS

As is clear from Fig. 3 and 4, the supersymmetric parameter space will mostly remain below the sensitivity level of the next generation of instruments. A few configurations are potentially detectable provided that the ACT threshold is decreased down to 50 GeV. If neutralinos are clumped inside the dark matter halo of M87, the situation considerably improves. As the gamma–ray production rate goes as the square of the density, neutralinos annihilate more efficiently as they condense. That overall effect may be described by the clumpiness factor \mathcal{C} , which is defined as the increase of the global annihilation rate that results from a possible clumpy structure of the dark matter distribution.

Neutralinos are cold dark matter species. As such, they exhibit density fluctuations

$$\left(\frac{\delta\rho}{\rho}\right)^2 \sim |\delta_k|^2 k^3 ,$$
(30)

that are related to the comoving wave vector k through [31]

$$|\delta_k|^2 \equiv P(k) = \frac{Ak}{(1 + \alpha k + \beta k^{1.5} + \gamma k^2)^2}$$
 (31)

with $\alpha = 1.71 \times l$, $\beta = 9 \times l^{1.5}$ and $\gamma = l^2$ where $l = (\Omega h^2)^{-1}$. Normalization to $\sigma_8 = 0.8$ gives $A = 2.82 \times 10^6 \,\mathrm{Mpc}^4$ when $\Omega = 1$ and h = 0.5. In a restricted wavelength range, it is approximated by a power law

$$P(k) \propto k^n$$
 (32)

The power spectrum P(k) of density fluctuations behaves as k^{-3} on small scales, *i.e.*, for structures typically lighter than $10^8~M_{\odot}$. As regards a possible clumpy structure of the halo around M87, the relevant mass range extends from

 $M_{\rm i} \sim 10^8~M_{\odot}$ up to $M_{\rm s} \sim 10^{13}~M_{\odot}$. The corresponding spectral index n goes from -2.6 to -2.1. As shown below, structures smaller than $M_{\rm i}$ turn out to all have the same density. They contribute identically to the clumpiness factor \mathcal{C} . There is no larger structure than the halo itself whose mass $M_{\rm s}$ reaches $10^{13}~M_{\odot}$ in the inner 100 kpc. Because the comoving wave vector k scales as $M^{-1/3}$, neutralino density fluctuations depend on both the scale M and the redshift z as

$$\frac{\delta\rho}{\rho} \propto (1+z)^{-1} M^{-(n+3)/6}$$
 (33)

The redshift factor $(1+z)^{-1}$ is typical of the $t^{2/3}$ growth of density fluctuations in a flat matter-dominated universe. Notice that small scale perturbations, for which n=-3, all become non-linear at the same time. Their subsequent collapse leads to virialized structures whose densities have been enhanced by a factor of ~ 180 with respect the epoch of formation, when $\delta \rho/\rho$ reached unity. Small scale dark matter clumps all have therefore the same density today. The formation redshift of larger structures behaves as

$$(1+z_{\rm F}) \propto M^{-(n+3)/6}$$
 , (34)

so that today, neutralino clumps with mass above $\sim 10^8~M_{\odot}$ have a density

$$\rho(M) \propto 180 \ (1 + z_{\rm F})^3 \propto M^{-(n+3)/2} \ .$$
 (35)

The density $\rho(M_{\rm s})$ of the largest possible clump should be comparable to the average dark matter density $\rho_{\rm DM}$ in the halo around M87. The distribution of clumps should follow the Press–Schechter's law

$$\frac{dN}{dM} = \frac{M_0}{M^2} \ . \tag{36}$$

The normalization mass M_0 obtains from the requirement that the clumps make up a fraction f of the halo. Disregarding for the moment clumps with mass less than $10^8 M_{\odot}$, we get

$$M_0 = \frac{f M_{\rm s}}{\ln{(M_{\rm s}/M_{\rm i})}} \ . \tag{37}$$

Some clumps are actually destroyed through the tidal stripping resulting from both their mutual interactions and the action of the gravitational field of M87. Just like globular clusters orbiting the Milky Way, they evaporate so that a fraction f only of the initial population is expected to survive. Inside a clump with mass M, the annihilation rate of neutralinos is $\langle \sigma v \rangle \{\rho(M)/m_\chi\}^2$ per unit volume. A net number $\langle \sigma v \rangle \rho(M) M/m_\chi^2$ of annihilations take place in the clump per unit time. We infer that the total annihilation rate of clumped neutralinos is obtained from the convolution

$$\Gamma_{\text{clump}} = \int_{M_{\text{i}}}^{M_{\text{s}}} \frac{\langle \sigma v \rangle}{m_{\chi}^2} \rho(M) M \frac{dN}{dM} dM . \tag{38}$$

Taking into account the mass-density relation (35) as well as the mass distribution (36) of the clumps, we readily infer the rate

$$\Gamma_{\text{clump}} = \frac{\langle \sigma v \rangle}{m_{\chi}^2} \rho_{\text{DM}} M_0 \int_{M_i}^{M_s} \left(\frac{M}{M_s}\right)^{-(n+3)/2} \frac{dM}{M} . \tag{39}$$

This may be compared to what a homogeneous distribution would yield

$$\Gamma_{\text{hom}} = \frac{\langle \sigma v \rangle}{m_{\chi}^2} \rho_{\text{DM}} M_{\text{s}} . \tag{40}$$

The clumpiness factor C may be understood as the enhancement ratio $\Gamma_{\text{clump}}/\Gamma_{\text{hom}}$. Clumps span less space than if their matter was homogeneously distributed. In their interiors, neutralinos nevertheless annihilate much more efficiently. The net effect is the increase

$$C = \left(\frac{2}{n+3}\right) \left(\frac{f}{\ln\left(M_{\rm s}/M_{\rm i}\right)}\right) \left[\left(\frac{M_{\rm s}}{M_{\rm i}}\right)^{(n+3)/2} - 1\right] . \tag{41}$$

This expression gives $\mathcal{C} \approx 34 \, f$ for n = -2.1 and $\mathcal{C} \approx 4 \, f$ for n = -2.6. With a general power spectrum P(k), this expression reads

$$C = \left(\frac{f}{\ln\left(M_{\rm s}/M_{\rm i}\right)}\right) \int_{M_i}^{M_s} \left(\frac{M}{M_s}\right)^{-3/2} \left(\frac{P(M)}{P(M_s)}\right)^{3/2} \frac{dM}{M} \tag{42}$$

where we go from P(k) to P(M) through

$$k = \left(\frac{M}{M_{\odot}} \frac{G}{3H_0^2 \pi^2}\right)^{-1/3} \tag{43}$$

The CDM power spectrum leads to $C \approx 13 f$. If we now assume that most of the clumps are small and that their mass does not exceed $M_i = 10^8 M_{\odot}$, we find

$$\Gamma_{\text{clump}} = \frac{\langle \sigma v \rangle}{m_{\chi}^2} \rho(M_{\text{i}}) \int M \, dN \quad .$$
 (44)

If that population of light clumps accounts for a fraction f of the dark matter halo around M87, the previous relation translates into

$$\Gamma_{\text{clump}} = \frac{\langle \sigma v \rangle}{m_{\chi}^2} \, \rho(M_{\text{i}}) \, f \, M_{\text{s}} \, .$$
 (45)

The clumpiness factor becomes

$$C = f \frac{\rho(M_i)}{\rho(M_s)} = f \left(\frac{M_s}{M_i}\right)^{(n+3)/2} , \qquad (46)$$

in the case of a power-law spectrum or more generally

$$C = f \left(\frac{M_{\rm s}}{M_{\rm i}}\right)^{3/2} \left(\frac{P(M_i)}{P(M_s)}\right)^{3/2} , \qquad (47)$$

It reaches a value of $C \sim 40 f$ for the CDM power spectrum. Varying the fraction f between 0.1 and 1, we conclude that depending on the typical size of the clumps, the gamma–ray production rate may be enhanced by factors as large as 40. The lower solid lines in Fig. 3 show the sensitivity limits of ACTs assuming that C = 40. A Čerenkov telescope operating with a 50 GeV threshold would detect a neutralino–induced gamma–ray emission from the giant elliptical galaxy M87 for a part of the supersymmetric configurations outlined in the upper–left panel of Fig. 3. Even with the annihilation rate enhanced by a factor of 40, the gamma ray lines are out of reach.

ACKNOWLEDGMENTS

We wish to thank E. Nuss for the information which he provided to us as well as for stimulating discussions. We thank D. Finkbeiner for assistance in using the dust maps of [20]. During his visits to Annecy, E. Baltz has been supported in part by the Programme National de Cosmologie. At Berkeley E. Baltz is supported by grants from NASA and DOE.

- [1] H.-U. Bengtsson, P. Salati and J. Silk, Nucl. Phys. B **346**, 129 (1990).
- [2] V. Berezinsky, A. Bottino and G. Mignola, Phys. Lett. B **325**, 136 (1994).
- [3] G. Jungman, M. Kamionkowski and K. Griest, Phys. Rep. 267, 195 (1996).
- [4] L. Bergstrom, P. Ullio and J. Buckley, Astropart. Phys. 9, 137 (1998).
- [5] P. Chardonnet et al., Astrophys. J. **454**, 774 (1995).
- [6] C.L. Sarazin, Rev. Mod. Phys. 58, 1 (1986).

- [7] J.C. Tsai, Astrophys. J. 413, L59 (1993).
- [8] A. Burkert, Astrophys. J. 474, L99 (1997).
- [9] J. S. Gallagher and R. F. G. Wyse, PASP **106** 1225 (1994).
- [10] M. Irwin and D. Hatzidimitriou, Mon. Not. R. Astron. Soc. 277 1354 (1995).
- [11] I. R. King, Astronomical J. **70**, 376 (1965).
- [12] I. R. King, Astronomical J. 67, 471 (1962).
- [13] K. S. Oh, D. N. C. Lin and S. J. Aarseth, Astrophys. J. 442, 142 (1995).
- [14] T. Sjöstrand, Comm. Phys. Comm. 82, 74 (1994); T. Sjöstrand, PYTHIA 5.7 and JETSET 7.4. Physics and Manual, CERN-TH.7112/93, hep-ph/9508391 (revised version).
- [15] F. A. Aharonian, W. Hofmann, A. K. Konopelko and H. J. Völk, Astropart. Phys. 6, 343 (1997) and Astropart. Phys. 6, 369 (1997).
- [16] J. Nishimura et al., Astrophys. J. 238, 394 (1980).
- [17] M. J. Ryan, J. F. Ormes and V. K. Balasubrahmanyan, Phys. Rev. Lett. 28, 985 (1972).
- [18] E. Nuss, private communication (1999).
- [19] P. Sreekumar et al., Astrophys. J. **494**, 523 (1998).
- [20] D. J. Schlegel, D. P. Finkbeiner and M. Davis, Astrophys. J. 500, 525 (1998).
- [21] J. Edsjö and P. Gondolo, Phys. Rev. D 56, 1879 (1997).
- [22] J. Edsjö, PhD Thesis, Uppsala University, hep-ph/9704384.
- [23] M. Drees, M. M. Nojiri, D.P. Roy and Y. Yamada, Phys. Rev. D 56, 276 (1997); D. Pierce and A. Papadopoulos, Phys. Rev. D 50, 565 (1994) and Nucl. Phys. B 430, 278 (1994); A. B. Lahanas, K. Tamvakis and N. D. Tracas, Phys. Lett. B 324, 387 (1994).
- [24] M. Carena, J. R. Espinosa, M. Quirós and C. E. M. Wagner, Phys. Lett. B 355, 209 (1995).
- [25] Talk by J. Carr, March 31, 1998, http://alephwww.cern.ch/ALPUB/seminar/carrlepc98/index.html Preprint ALEPH 98-029, 1998 winter conferences, http://alephwww.cern.ch/ALPUB/oldconf/oldconf.html
- [26] M. S. Alam et al. (CLEO Collaboration), Phys. Rev. Lett. 71, 674 (1993) and Phys. Rev. Lett. 74, 2885 (1995).
- [27] P. Gondolo and G. Gelmini, Nucl. Phys. B 360, 145 (1991).
- [28] D. N. Schramm and M. S. Turner, Rev. Mod. Phys. 70, 303 (1998).
- [29] http://www-hfm.mpi-hd.mpg.de/HESS/HESS.html
- [30] http://pursn3.physics.purdue.edu/veritas/
- [31] M. Davis, G. Efstathiou, C. S. Frenk, and S. D. M. White, Astrophys. J. 292, 371 (1985)